Oxygen reduction on bimodal nanoporous palladium-copper catalyst synthesized using sacrificial nanoporous copper

Naoki Miyazawa, Masataka Hakamada*, Yuto Sato and Mamoru Mabuchi

Department of Energy Science and Technology, Graduate School of Energy Science, Kyoto University, Yoshidahonmachi, Sakyo, 606-8501 Kyoto, Japan

* Corresponding author. E-mail: hakamada.masataka.3x@kyoto-u.ac.jp (M. Hakamada).

Abstract

Nanoporous copper (NP-Cu), as a sacrificial support, was used for the synthesis of bimodal nanoporous palladium-copper (BNP-PdCu) for oxygen reduction reaction (ORR) electrodes in fuel cells. The catalytic performance of BNP-PdCu in ORR per electrochemical surface area was enhanced by the dissolution and removal of supporting NP-Cu, which indicates that the intrinsic catalytic properties of palladium are improved by the proposed synthesis strategy including galvanic replacement of copper with palladium, following copper dissolution. Cu remained on Pd surfaces even after dissolution of Cu. Additionally, significant local lattice contraction was observed at the ligament surface. First-principles calculations on the adsorbing oxygen species on Pd show that both lattice contraction and alloying with copper increase the binding energies of oxygen species to the Pd surface. The high ORR activity of the present BNP-PdCu is suggested to be mainly due to the Cu-ligand effect.

Keywords: Pd; nanostructure; surface reaction

Introduction

Catalytic electrodes in fuel cells are typically made from platinum, which is rare in the earth's crust. The scarcity is the main reason for the high and fluctuating price of platinum and prevents the wide application of fuel cells. The performance of fuel cells is often governed by the oxygen-reduction reaction (ORR) at an air electrode.[1] Thus, various studies on the optimization of catalytic platinum electrodes have been conducted.[1–3]

Another effort is the substitution of platinum by other elements. Palladium is one possible element for the substitution because the electronic structure of palladium is similar to that of platinum, which is clearly understood from the periodic table. From the viewpoint of surface area, nanostructuring of palladium is a key strategy for the efficient production of the air electrode. However, it has been found that the catalytic properties of palladium for ORR are much lower than those of platinum.[4] For this reason, many studies have been carried out to achieve a better catalytic performance of palladium than platinum by efforts such as nanoparticle formation[5] and alloying.[6]

Nanoporous metal synthesis, by dealloying or selective dissolution of one element from a binary alloy, has been developed after a report in 2001[7] and is now another technology for nanostructuring. Dealloying can create three-dimensional nanoporous structures in various metals, which generate pores and ligaments in the nanometer-size range.[8,9] It is well known that nanoporous Raney copper can be synthesized by dealloying Cu–Al alloys in alkaline solutions.[10] Nanoporous copper (NP-Cu) can also be produced by dealloying ductile Cu–Mn alloys.[11–13] Manganese is easy to dissolve even in neutral solution;[14] thus the precursor Cu–Mn alloys may be favorable for efficient production of NP-Cu.

Noble metals, including palladium, can be deposited in the form of a dense film or fine

particles on copper by electroless plating or galvanic replacement.[15–17] Thus, nanoporous palladium with a skeletal structure replicated from NP-Cu can be produced by electroless plating of palladium on NP-Cu. The supporting NP-Cu can be removed readily by HNO_3 which dissolves copper selectively, and leaves bimodal nanoporous platinum with residual copper (BNP-PdCu) (Fig. 1). In addition, the distribution of lattice spacing from surface to core is significantly varied in nanostructured materials including nanoporous metals,[18,19] causing peculiar surface chemistry.[18,20–22] In this study, BNP-PdCu for ORR catalysts was fabricated by electroless plating of palladium on the sacrificial NP-Cu and subsequent dissolution of NP-Cu. We focus on high ORR activity per surface area of fabricated BNP-PdCu catalysts, using first-principles calculations on the adsorption of oxygen species on palladium surfaces.

Results

STEM images (Fig. 2) indicated the bimodal structure of the BNP-PdCu after dissolution of copper. The nanoporous hollow structure with an average pore diameter of 23 nm (Fig. 2(a)), which is replicated from NP-Cu (Fig. 1(b)), was composed of finer Pd aggregates with 5–10-nm diameters (Fig. 2(b)), forming the bimodal nanoporous structure. STEM-EDXS revealed that Cu remained even after dissolution by HNO_3, although Cu and Pd exhibited a homogeneous distribution without surface segregation (Fig. 2(c)). HR-TEM observation (Fig. 2(d)) showed significant local lattice contraction at ligament surfaces. The remaining Cu in the sample after dissolution by HNO_3 was confirmed by EDXS (Fig. 3(a)), where the atomic ratio of Cu/Pd was 0.25 before dissolution and 0.15 after dissolution. On the other hand, manganese was not detected by EDXS and ICP-AES in BNP-PdCu before and after the dissolution of copper. Thus, the contribution of manganese was eliminated in the following

discussion on the catalytic properties of the BNP-PdCu samples.

XRD patterns of BNP-PdCu before and after copper dissolution are shown in Fig. 3(b). Before copper dissolution, the broad peaks for palladium were detected with minor peaks for metallic copper. The absence of copper peaks in the XRD pattern even before dissolution of copper suggested that a considerable amount of copper was removed at the stage of the displacement deposition of palladium. Comparison of the present Cu/Pd composition ratio with the case of Cu/Pt[23] also suggested the removal of copper during the displacement deposition of palladium. The broad peaks for palladium were detected whereas no copper was detected by XRD after dissolution by HNO_3. Pd remained undissolved after immersion in HNO_3 for removal of skeletal Cu. An inspection of the XRD patterns showed no significant peak shift of Pd (Table I), compared with the case of Cu/Pt.[23]

CV curves for BNP-PdCu before and after copper dissolution (Fig. 4(a)) were typical for palladium[24–26] with peaks for oxygen desorption. Copper dissolution by HNO_3 caused no significant change in the redox process during CV scanning. On the other hand, no redox peaks from copper were detected. Considering that elemental mapping in TEM for BNP-PdCu showed no clear segregation of palladium and copper (Fig. 2(c)), one can suggest that the change in the chemical state of surface Cu by alloying with Pd and/or that the surface coverage by Cu is not so high.

The ORR activity of the BNP-PdCu samples was examined by RDE (Fig. 4(b)). In the polarization curves, the current density at a high potential of 1.1 V was almost independent of the electrode rotation rate, which corresponded to the kinetic region of the ORR. As the potential was decreased from 1.1 V, transitional regions from a kinetic- to a diffusion-

controlled reaction rate were observed, with a lower current density at a higher electrode rotation rate. Below 0.4 V, the current density was almost constant and a diffusion-controlled reaction occurred.

The specific activities of BNP-PdCu before and after dissolution of copper were 0.32 and 0.61 mA cm^{-2}, respectively, according to the RDE results. These values were significantly higher than those of the conventional Pd/C catalyst and comparable with the values reported recently for other nanostructured Pd-based alloys.[27–31] On the other hand, the mass activity of BNP-PdCu before and after copper dissolution was 0.023 and 0.034 A mg_{Pd}^{-1}, respectively. The copper dissolution increased the specific activity of the BNP-PdCu. A higher activity per ECSA (not per mass or geometric area) for BNP-PdCu after copper dissolution meant that the copper dissolution enhanced the intrinsic ORR catalytic nature of the palladium.

Discussion

In the case of platinum, which has been examined intensively in previous studies, lattice straining affects the overall catalytic performance for ORR in platinum;[32–34] lattice contraction is favorable for efficient ORR catalysis on platinum.[32] However, it has been reported that both lattice contraction[35–37] and expansion[27] in palladium catalysts enhances the overall catalytic performance for ORR. XRD analyses revealed that the apparent lattice constants of palladium in BNP-PdCu are close to those for bulk palladium (Table I), which is in contrast with the case of BNP-Pt[23]. However, HR-TEM of BNP-PdCu showed significant local lattice contraction at ligament surfaces, as exemplified in Fig. 2(d). That is, the lattice spacing at the surface of ligaments is smaller than that in the bulk part of ligaments. This lattice disorder at the surface of nanoligaments is often observed in nanoporous metals and is attributed to the complex three-dimensional nanostructure with positive and negative

curvatures.[18,19,22] The present BNP-PdCu is replicated from NP-Cu; therefore, the lattice disorder is likely to be prominent, considering the increased complexity in the replicated BNP structure.

It is known that the binding of oxygen species to Pd surfaces is too strong and it is difficult to cause further reduction of the oxygen species to form water on Pd surfaces.[46,47] Therefore, a weak oxygen binding is desirable to balance the rates of electron transfer/O−O bond breaking and removal of O species from Pd surfaces.[27] As shown above, Cu remained on the BNP-PdCu surface even after dissolution by HNO_3, in addition, a lattice disorder was generated at its surface. Therefore, it is suggested that the Cu-ligand effect and/or the strain effect led to the high ORR activity of BNP-PdCu. To obtain insights in the origins of the high ORR activity of BNP-PdCu, the binding energies of O and O_2 to Pd and PdCu were calculated. The results are shown for Pd in Fig. 5 and for PdCu in Fig. 6. The most stable binding sites for Pd were the fcc for O and the t-f-b for O_2, regardless of the strain. However, the most stable binding sites for PdCu were different from those for Pd. The most stable binding sites and binding energies are listed in Table II. Table II shows that the binding energies of the oxygen species are increased (negatively decreased) by the contraction strain for Pd, while the binding energies are decreased (negatively increased) by the expansion strain, which indicates that the contraction strain enhances the desorption of oxygen species on Pd although the expansion strain disturbs the desorption. Thus, the contraction strain leads to the enhanced ORR activity of Pd. In addition, Table II shows that the binding energies are increased by the addition of Cu, regardless of the strain. This suggests that the ORR activity of Pd is enhanced owing to the Cu-ligand effect. The Cu-ligand effect can significantly enhance the ORR activity of Pd because the binding energies are largely increased by the addition of Cu.

The densities of states (DOS) for a palladium atom of the Pd (PdCu) surface binding to an oxygen atom are shown in Fig. S1 in Supplementary Material. The electronic states for Pd were hardly changed by the presence of strains, which corresponds to the result that the strain had little effect on the d-band center for Pd (Table II). However, the electronic states were changed by the presence of Cu (see Fig. S1(a) and (d)). Both the downshift and upshift of the d-band center were caused by the addition of Cu (Table II). Thus, the variation in binding energy by the addition of Cu cannot be explained only from the viewpoint of the d-band center. The charge density distribution between the palladium and oxygen atoms is shown in Fig. 7. The charge density between the palladium and oxygen atoms was lower for PdCu than for Pd. Therefore, it is proposed that the binding energy increased by the addition of Cu is related to the reduced charge density.

As shown above, the contraction strain and the addition of Cu enhance the ORR activity of Pd. Hence, the high ORR activity of BNP-PdCu may be related to both the strain effect and the Cu-ligand effect. The present experimental results showed that the ORR activity was enhanced by the dissolution of Cu, although the contraction strain might be reduced and the amount of Cu on Pd was reduced by the dissolution. The Pd surface that is covered by Cu before the dissolution cannot provide the sites for ORR. In such a case, only the strain effect enhances the ORR activity because the Pd surface that is not covered by Cu provides the sites for ORR. After the dissolution, however, not only the strain effect but also the Cu-ligand effect enhances the ORR activity because Cu remains on the Pd surface. It is therefore suggested that the high ORR activity of BNP-Pd mainly arises from the Cu-ligand effect.

Conclusions

Efficient ORR BNP-PdCu catalysts were fabricated by using NP-Cu as a sacrificial metallic

support. Cu remained on Pd surfaces even after dissolution of Cu. The high ORR activity of BNP-PdCu was suggested to mainly arise from the Cu-ligand effect.

Experimental methods

Copper-manganese alloy ingots with the composition of $Cu_{0.3}Mn_{0.7}$ were fabricated by the arc melting of pure copper and manganese (Nilaco, Tokyo, Japan) in an Ar atmosphere. After heating at 1123 K for 24 h in an Ar atmosphere, the button-shaped alloy ingot was water-quenched,[40] followed by cold rolling to 0.2-mm thickness.

Dealloying to fabricate NP-Cu was conducted by free corrosion of the rolled $Cu_{0.3}Mn_{0.7}$ sheet in 1 mol L^{-1} HCl for 24 h, where manganese was dissolved selectively and copper formed a nanoporous structure spontaneously (Fig. 1(b)).[11–13] After recovery by percolation and washing in pure water, the NP-Cu was pulverized manually in an agate bowl.

NP-Cu (0.05 g) was mixed with 5 wt% Nafion ethanolic solution (1 g) and of water (5 g). After homogenization in an ultrasonic bath, the suspension was fixed on a glassy carbon (GC) rotation disk electrode (RDE) with 5-mm diameter. The displacement deposition of palladium on the fixed NP-Cu was conducted by immersing the GC RDE in diluted HCl containing 0.1 mol L^{-1} $PdCl_2$ at 273 K for 1 h at 600 rpm.[41] Thus, the GC electrode included NP-Cu with a fine palladium deposition; the bimodal nanoporous structure of palladium supported on NP-Cu was expected to form already at this step (Fig. 1(a)). The GC electrode that included BNP-PdCu was immersed in 0.1 mol L^{-1} HNO_3 for 18 h to dissolve the supporting copper.

We conducted cyclic voltammetry (CV) at room temperature by using the GC electrode loaded with BNP-PdCu as a working electrode. To evaluate the electrochemical surface area

(ECSA) of the BNP-PdCu samples, CV was conducted in degassed 0.1 mol L^{-1} H_2SO_4 with a scan rate of 10 mV s^{-1}. A reversible hydrogen electrode (RHE) and Pt wire were used as a reference and counter electrode, respectively. For electrochemical cleaning, CV was repeated until a steady current-potential cyclic curve was attained. The charge (Q_O) associated with the reduction of oxidized monolayer was calculated by using the cathodic peak between 0.6 and 0.8 V (vs. RHE), which was then converted to the ECSA (A) of the sample:[42]

$$A_{\text{sample}}/A_{\text{bulk}} = Q_{O,\text{sample}}/Q_{O,\text{bulk}} \quad (1)$$

where the subscripts "sample" and "bulk" represent the BNP-PdCu and bulk palladium, respectively.

The working GC-RDE-loaded BNP-PdCu was rotated for ORR activity measurements during CV in an electrolyte of O_2-saturated 0.1 mol L^{-1} H_2SO_4 with a scan rate of 10 mV s^{-1}. The kinetically-controlled current i_K, which is an index of the ORR activity of the BNP-PdCu, was calculated according to:

$$1/i = 1/i_K + 1/B\omega^{1/2} \quad (2)$$

where i is the measured current; B is a constant and ω is the RDE rotation speed. i_K was derived from the intersection at $\omega^{-1/2} = 0$ by the Koutechy–Levich plot of i^{-1} (at 0.70 V vs. RHE) against $\omega^{-1/2}$.[43]

Substances on the GC RDE were collected for SEM, scanning transmission electron microscopy (STEM) and high-resolution transmission electron microscopy (HR-TEM). Energy-dispersive X-ray spectroscopy (EDXS) was used for elemental analyses in the microscopic observations. X-ray diffraction (XRD) patterns of the samples were collected under a parallel-beam configuration. The concentrations of palladium and other elements in

the samples were determined by inductively-coupled plasma atomic emission spectroscopy (ICP-AES) after dissolving the samples in 20 mL of nitrohydrochloric acid.

Calculation methods

First-principles calculations on the adsorption of O and O_2 on (111) Pd and PdCu surfaces were carried out to understand the origins for the catalytic activity of BNP-PdCu. The first-principles calculations were performed within the framework of density functional theory[44,45] as implemented in the CASTEP code.[46] The plane-wave basis set was used to calculate the electronic properties, and the generalized gradient approximation of the Perdew-Burke-Ernzerhof[47] functional was used for the exchange-correlation potential for the structure optimizations. Ultrasoft pseudopotentials[48] were used for all the elements in the calculations. We applied cutoff energies of 400 eV. The Brillouin zone was sampled using 5×5×1 Monkhorst-Pack *k*-point meshes.[49] Periodic boundary conditions were applied in the x, y and z directions.

Atomic models are shown in Fig. S2 in Supplementary Material. The rectangular cell consisted of 4 layers of the (111) plane of Pd with a vacuum gap of 15 Å between repeated slabs (Fig. S2(a)). The PdCu model was constructed by substituting one Pd atom at each layer except the top lay with one Cu atom to avoid direct reaction of a Cu atom with an oxygen atom (Fig. S2(b)). A 2% tensile and compressive strain was applied parallel to the exposed surface to identify the strain effects. All cells were constructed from 2 × 2 surface unit cells. The top three layers were relaxed while the bottom layer was frozen during geometry optimization calculations. The binding energy of an oxygen species to a substrate (E_{b}) can be given by:

$$E_{\mathrm{b}} = E_{\mathrm{substrate+oxygen}} - E_{\mathrm{substrate}} - E_{\mathrm{oxygen}} \quad (3)$$

where $E_{\mathrm{substrate+oxygen}}$ is the internal energy of an oxygen species-binding substrate, $E_{\mathrm{substrate}}$ is the internal energy of a substrate and E_{oxygen} is the internal energy of an oxygen species. The most stable binding site of an oxygen species was defined as the site where the binding energy was the lowest among the various binding sites shown in Fig. S2, based on a previous study.[50]

Acknowledgments

TEM and STEM observations were conducted at the Kyoto University Nano Technology Hub in the "Nanotechnology Platform Project" sponsored by the Ministry of Education, Culture, Sports, Science and Technology (MEXT), Japan. Computation time for first-principles calculations was provided by the SuperComputer System, Institute for Chemical Research, Kyoto University. M. H. acknowledges financial support by JGC-S Scholarship Foundation.

Supplementary Material

To view supplementary material for this article, please visit [URL to be provided].

References

[1] I. E. L. Stephens, A. S. Bondarenko, U. Grønbjerg, J. Rossemeisl, and I. Chorkendorff: Understanding the electrocatalysis of oxygen reduction on platinum and its alloys. *Energy Environ. Sci.* **5**, 6744–6762 (2012).

[2] K. Wikander, H. Ekström, A. E. C. Palmqvist, and G. Lindbergh: On the influence of Pt particle size on the PEMFC cathode performance. *Electrochem. Acta* **52**, 6848–6855 (2007).

[3] R. Chattot, O. L. Bacq, V. Beermann, S. Kühl, J. Herranz, S. Henning, L. Kühn, T. Asset,

L. Guétaz, G. Renou, J. Drnec, P. Bordet, A. Pasturel, A. Eychmüller, T. J. Schmidt, P. Strasser, L. Dubau, and F. Maillard: Surface distortion as a unifying concept and descriptor in oxygen reduction reaction electrocatalysis. *Nat. Mater.* **17**, 827–833 (2018).

[4] D. Jung, S. Beak, K. S. Nahm, and P. Kim: Enhancement of oxygen reduction activity by sequential impregnation of Pt and Pd on carbon support. *Korean J. Chem. Eng.* **27**, 1689–1694 (2010).

[5] S. Liu, X. Mu, H. Duan, C. Chen, and H. Zhang: Pd nanoparticle assemblies as efficient catalysts for the hydrogen evolution and oxygen reduction reactions. *Eur. J. Inorg. Chem.* **2017**, 535–539 (2017).

[6] M. Neergat, V. Gunasekar, and R. Rahul: Carbon-supported Pd–Fe electrocatalysts for oxygen reduction reaction (ORR) and their methanol tolerance. *J. Electroanal. Chem.* **658**, 25–32 (2011).

[7] J. Erlebacher, M. J. Aziz, A. Karma, N. Dimitrov, and K. Sieradzki: Evolution of nanoporosity in dealloying. *Nature* 410, 450–453 (2001).

[8] A. J. Forty: Corrosion micromorphology of noble metal alloys and depletion gilding. *Nature* **282**, 597–598 (1979).

[9] D. V. Pugh, A. Dursun, and S. G. Corcoran: Formation of nanoporous platinum by selective dissolution of Cu from $Cu_{0.75}Pt_{0.25}$. *J. Mater. Res.* **18**, 216–221 (2003).

[10] X. Kong, C. Ma, J. Zhang, J. Sun, J. Chen, and K. Liu: Effect of leaching temperature on structure and performance of Raney Cu catalysts for hydrogenation of dimethyl oxalate, *Appl. Catal. A-Gen.* **509**, 153–160 (2016).

[11] D. S. Keir and M. J. Pryor: The dealloying of copper-manganese alloys. *J. Electrochem. Soc.* **127**, 2138–2144 (1980).

[12] U.-S. Min and J. C. M. Li: The microstructure and dealloying kinetics of a Cu-Mn alloy. *J. Mater. Res.* **9**, 2878–2883 (1994).

[13] J. R. Hayes, A. M. Hodge, J. Biener, A. V. Hamza, and K. Sieradzki: Monolithic nanoporous copper by dealloying Mn–Cu. *J. Mater. Res.* **21**, 2611– 2616 (2006).

[14] M. Hakamada and M. Mabuchi: Preparation of nanoporous Ni and Ni-Cu by dealloying of rolled Ni-Mn and Ni-Cu-Mn alloys. *J. Alloy. Compd.* **485**, 583–587 (2009).

[15] A. Liu, H. Geng, C. Xu, and H. Qiu: A three-dimensional hierarchical nanoporous PdCu alloy for enhanced electrocatalysis and biosensing. *Anal. Chem. Acta* **703**, 172–178 (2011).

[16] B. Rezaei, E. Havakeshian, and A. A. Ensafi: Fabrication of a porous Pd film on nanoporous stainless steelusing galvanic replacement as a novel electrocatalyst/electrode design for glycerol oxidation. *Electrochem. Acta* **136**, 89–96 (2014).

[17] J.-B. Raoof, S. R. Hosseini, R. Ojani, and S. Aghajani: Fabrication of bimetallic Cu/Pd particlesmodified carbon nanotube paste electrode and its use towards formaldehyde electrooxidation. *J. Mol. Liq.* **204**, 106–111 (2015).

[18] M. Hakamada, H. Nakano, T. Furukawa, M. Takahashi, and M. Mabuchi: Hydrogen storage properties of nanoporous palladium fabricated by dealloying. *J. Phys. Chem. C* **114**, 868–873 (2010).

[19] C. Mahr, K. Müller-Caspary, M. Graf, A. Lackmann, T. Grieb, M. Schowalter, F. F. Krause, T. Mehrtens, A. Wittstock, J. Weissmüller, and A. Rosenauer: Measurement of local crystal

lattice strain variations in dealloyed nanoporous gold. *Mater. Res. Lett.* **6**, 84–92 (2018).

[20] M. Hakamada, F. Hirashima, and M. Mabuchi: Catalytic decoloration of methyl orange solution by nanoporous metals. *Catal. Sci. Technol.* **2**, 1814–1817 (2012).

[21] M. Miyazawa, M. Hakamada, and M. Mabuchi: Antimicrobial mechanisms due to hyperpolarization induced by nanoporous Au. *Sci. Rep.* **8**, 3870 (2018).

[22] T. Fujita, P. Guan, K. McKeena, X. Y. Lang, A. Hirata, L. Zhang, T. Tokunaga, S. Arai, Y. Yamamoto, N. Tanaka, Y. Ishikawa, N. Asao, Y. Yamamoto, J. Erlebacher, and M. W. Chen: Atomic origins of the high catalytic activity of nanoporous gold. *Nat. Mater.* **11**, 775–780 (2012).

[23] M. Hakamada, Y. Sato, and M. Mabuchi: Bimodal nanoporous platinum on sacrificial nanoporous copper for catalysis of the oxygen-reduction reaction. *MRS Commun.* **9**, 292–297 (2019).

[24] W. Xiao, M. A. L. Cordeiro, M. Gong, L. Han, J. Wang, C. Bian, J. Zhu, H. L. Xin, and D. Wang: Optimizing the ORR activity of Pd based nanocatalysts by tuning their strain and particle size. *J. Mater. Chem. A* **5**, 9867–9872 (2017).

[25] R. Rahul, R. K. Singh, B. Bera, R. Devivaraprasad, and M. Neergat: The role of surface oxygenated-species and adsorbed hydrogen in the oxygen reduction reaction (ORR) mechanism and product selectivity on Pd-based catalysts in acid media. *Phys. Chem. Chem. Phys.* **17**, 15146–15155 (2015).

[26] Y. H. Xue, L. Zhang, W. J. Zhou and S. H. Chan. *Int. J. Hydrogen Energy* **39**, 8449–8456 (2014).

[27] M. Wang, X. Qin, K. Jiang, Y. Dong, M. Shao, and W.-B. Cai: Electrocatalytic activities of oxygen reduction reaction on Pd/C and Pd–B/C catalysts. *J. Phys. Chem. C* **121**, 3416–3423 (2017).

[28] D. Park, M. S. Ahmed, and S. Jeon: Covalent functionalization of graphene with 1,5-diaminonaphthalene and ultrasmall palladium nanoparticles for electrocatalytic oxygen reduction. *Int. J. Hydrogen Energy* **42**, 2061–2070 (2017).

[29] S. Salomé, A. M. Ferraria, A. M. Botelho do Rego, F. Alcaide, O. Savadogo, and R. Rego: Enhanced activity and durability of novel activated carbon-supported PdSn heat-treated cathode catalyst for polymer electrolyte fuel cells. *Electrochem. Acta* **192**, 268–282 (2016)

[30] Y. Holade, C. Canaff, S. Poulin, T. W. Napporn, K. Servat, and K. B. Kokoh: High impact of the reducing agent on palladium nanomaterials: new insights from X-ray photoelectron spectroscopy and oxygen reduction reaction. *RSC Adv.* **6**, 12627–12637 (2016).

[31] J. Begum, M. S. Ahmed, S. Cho, and S. Jeon: Freestanding palladium nanonetworks electrocatalyst for oxygen reduction reaction in fuel cells. *Int. J. Hydrogen Energy* **43**, 229–238 (2018).

[32] P. Strasser, S. Koh, T. Anniyev, J. Greeley, K. More, G. Yu, Z. Liu, S. Kaya, D. Nordlund, H. Ogasawara, M. F. Toney, and A. Nilsson: Lattice-strain control of the activity in dealloyed core-shell fuel cell catalysts. *Nat. Chem.* **2**, 454–460 (2010).

[33] F. M. F. Rhen and C. McKeown: Enhanced methanol oxidation on strained Pt films. *J. Phys. Chem. C* **121**, 2556–2562 (2017).

[34] H. A. Gasteiger, S. S. Kocha, B. Sompalli, and F. T. Wagner: Activity benchmarks and

requirements for Pt, Pt-alloy, and non-Pt oxygen reduction catalysts for PEMFCs. *Appl. Catal. B-Environ.* **56**, 9–35 (2005).

[35] G. Jiang, H. Zhu, X. Zhang, B. Shen, L. Wu, S. Zhang, G. Lu, Z. Wu, and S. Sun: Core/shell face-centered tetragonal FePd/Pd nanoparticles as an efficient non-Pt catalyst for the oxygen reduction reaction. *ACS Nano* **9**, 11014–11022 (2015).

[36] H. Zhang, Q. Hao, H. Geng, and C. Xu: Nanoporous PdCu alloys as highly active and methanol-tolerant oxygen reduction electrocatalysts. *Int. J. Hydrogen Energy* **38**, 10029–10038 (2013).

[37] L. Liu, G. Samjeske, S. Nagamatsu, O. Sekizawa, K. Nagasawa, S. Takao, Y. Imaizumi, T. Yamamoto, T. Uruga, and Y. Iwasawa. Dependences of the oxygen reduction reaction activity of Pd–Co/C and Pd–Ni/C alloy electrocatalysts on the nanoparticle size and lattice constant. *Top. Catal.* **57**, 595–606 (2014).

[38] M. Shao: Palladium-based electrocatalysts for hydrogen oxidation and oxygen reduction reactions. *J. Power Sources* **196**, 2433−2444 (2011).

[39] M. H. Shao, T. Huang, P. Liu, J. Zhang, K. Sasaki, M. B. Vukmirovic, and R. R. Adzic: Palladium monolayer and palladium alloy electrocatalysts for oxygen reduction. *Langmuir* **22**, 10409−10415 (2006).

[40] H. Okamoto: Cu-Mn (Copper-Manganese). *J. Phase Equilib.* **19**, 180 (1998).

[41] E. J. Coleman and A. C. Co: Galvanic displacement of Pt on nanoporous copper: An alternative synthetic route for obtaining robust and reliable oxygen reduction activity. *J. Catal.* **316**, 191–200 (2014).

[42] S. Trasatti and O. A. Petrii: Real surface area measurements in electrochemistry. *J. Electroanal. Chem.* **327**, 353–376 (1992).

[43] L.-L. He, P. Song, A.-J. Wang, J.-N. Zheng, L.-P. Mei, and J.-J. Feng: A general strategy for the facile synthesis of AuM (M = Pt/Pd) alloyed flowerlike-assembly nanochains for enhanced oxygen reduction reaction. *J. Mater. Chem. A* **3**, 5352–5359 (2015).

[44] P. Hohenberg and W. Kohn: Inhomogeneous electron gas, Phys. Rev. 136, B864–B871 (1964).

[45] W. Kohn and L. J. Sham: Self-Consistent equations including exchange and correlation effects, *Phys. Rev.* **140**, A1133–A1138 (1965).

[46] M. C. Payne, M. P. Teter, D. C. Allan, T. A. Arias, and J. D. Joannopoulos: Iterative minimization techniques for ab initio total-energy calculations: molecular dynamics and conjugate gradients, *Rev. Mod. Phys.* **64**, 1045–1097 (1992).

[47] J. P. Perdew, K. Burke, and M. Ernzerhof: Generalized gradient approximation made simple, *Phys. Rev. Lett.* **77**, 3865–3867 (1996).

[48] D. Vanderbilt: Soft self-consistent pseudopotentials in a generalized eigenvalue formation, *Phys. Rev. B* **41**, 7892–7895 (1990).

[49] H. J. Monkhorst and J. D. Pack: Special points for Brillouin-zone integrations, *Phys. Rev. B* **13**, 5188–5192 (1976).

[50] Y. Xu, A. V. Ruban, and M. Mavrikakis: Adsorption and dissociation of O_2 on Pt-Co and Pt-Fe alloys. *J. Am. Chem Soc.* **126**, 4717–4725 (2004).

Tables

Table I. Lattice constants of palladium in bimodal nanoporous palladium-copper.

Plane index	Lattice constant a (nm) and change from that in bulk palladium ($a_{\text{bulk Pd}}$ = 3.890 nm)	
	Before Cu dissolution	After Cu dissolution
111	3.880 (−0.27%)	3.879 (−0.29%)
200	3.888 (−0.05%)	3.885 (−0.13%)
220	3.874 (−0.42%)	3.879 (−0.29%)
311	3.882 (−0.21%)	3.889 (−0.04%)
Average	3.881 (−0.24%)	3.883 (−0.19%)

Table II. Most stable binding sites, their binding energies and d-band centers by first-principles calculations on binding of O and O_2 to (111) Pd and PdCu surfaces.

System		Strain	Stable binding site	Binding energy (eV)	d-band center (eV)
Pd	O	0%	fcc	−5.05	−1.01
		+2%	fcc	−5.10	−1.01
		−2%	fcc	−4.99	−1.01
	O_2	0%	t-f-b	−1.44	−0.67
		+2%	t-f-b	−1.47	−0.59
		−2%	t-f-b	−1.39	−0.68
PdCu	O	0%	top1	−4.74	−1.10
		+2%	hcp3	−4.93	−0.99
		−2%	top3	−4.79	−0.97
	O_2	0%	t-f-bc	−1.27	−0.64
		+2%	t-f-bc	−1.43	−0.61
		−2%	t-b-tb	−1.29	−0.62

Figure captions

Figure 1. (Color online) (a) Schematic illustration of synthesis of bimodal nanoporous PdCu using nanoporous copper as a sacrificial support. (b) Scanning electron microscopy image of nanoporous copper fabricated by dealloying of Cu–Mn alloy.

Figure 2. (Color online) Scanning transmission electron microscopy images of bimodal nanoporous PdCu. (a), (b) and left panel in (c) are high-angle annular dark-field images, and the center and right panels in (c) show the elemental mapping by energy-dispersive X-ray spectroscopy. Arrows in (a) shows diameters of replicated pores from nanoporous copper. (d) High-resolution transmission electron microscopy image of bimodal nanoporous PdCu, showing surface lattice contraction.

Figure 3. (Color online) (a) Energy-dispersive X-ray spectroscopy results and (b) X-ray diffraction patterns of bimodal nanoporous PdCu before and after copper dissolution.

Figure 4. (Color online) (a) Cyclic voltammetry curves for bimodal nanoporous PdCu before and after copper dissolution. The scan rate was 10 mV s^{-1} and the electrolyte was 0.1 mol L^{-1} H_2SO_4. (b) Polarization curves for rotation disk electrodes that load bimodal nanoporous PdCu before and after copper dissolution. The scan rate was 10 mV s^{-1} and the electrolyte was 0.1 mol L^{-1} H_2SO_4.

Figure 5. (Color online) Binding energies of O and O_2 to Pd surface, (a) O binding energy at 0% strain for fcc, hcp and top sites, (b) O_2 binding energy at 0% strain for t-f-b, t-h-b and t-b-t sites, (c) O binding energy at 2% contraction strain for fcc, hcp and top sites, (d) O_2 binding energy at 2% contraction strain for t-f-b, t-h-b and t-b-t sites, (e) O binding energy at 2% expansion strain for fcc, hcp and top sites, (f) O_2 binding energy at 2% expansion

strain for t-f-b, t-h-b and t-b-t sites.

Figure 6. (Color online) Binding energies of O and O_2 to PdCu surface, (a) O binding energy at 0% strain for fcc, hcp and top sites, (b) O_2 binding energy at 0% strain for t-f-b, t-h-b and t-b-t sites, (c) O binding energy at 2% contraction strain for fcc, hcp and top sites, (d) O_2 binding energy at 2% contraction strain for t-f-b, t-h-b and t-b-t sites, (e) O binding energy at 2% expansion strain for fcc, hcp and top sites, (f) O_2 binding energy at 2% expansion strain for t-f-b, t-h-b and t-b-t sites.

Figure 7. (Color online) Charge density distribution between palladium and oxygen atoms, (a) Pd surface with 0% strain, (b) Pd surface with 2% contraction strain and (c) PdCu surface with 0% strain.

(a)

1. Nanoporous Cu

2. Galvanic replacement by Pd

3. Cu dissolution

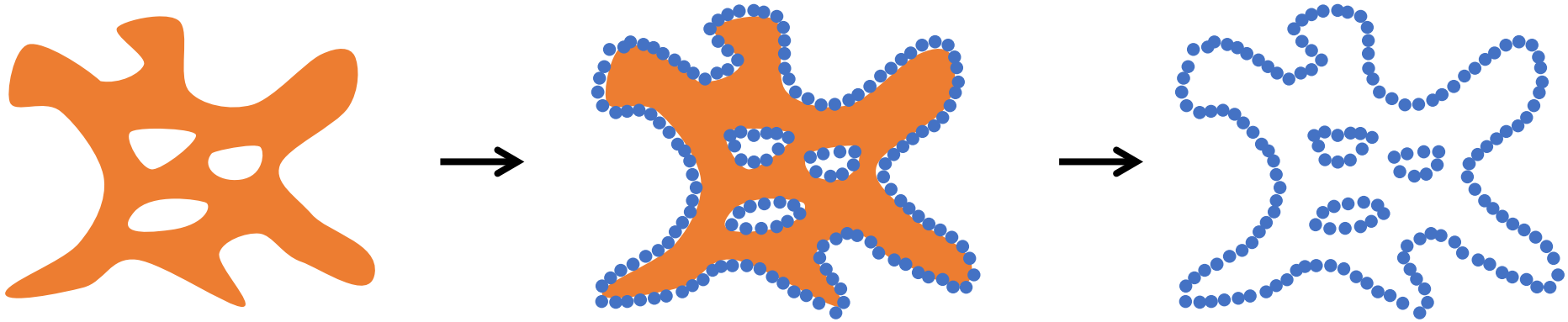

(b)

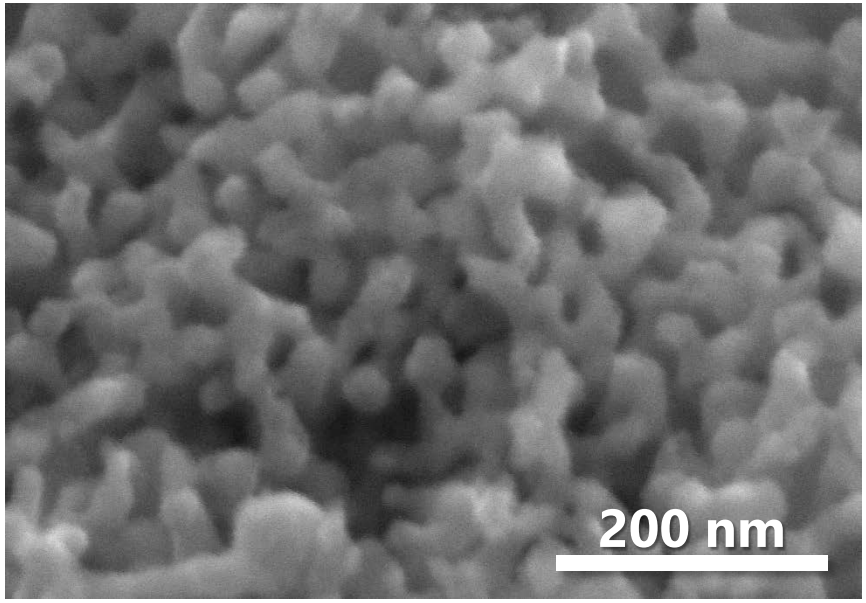

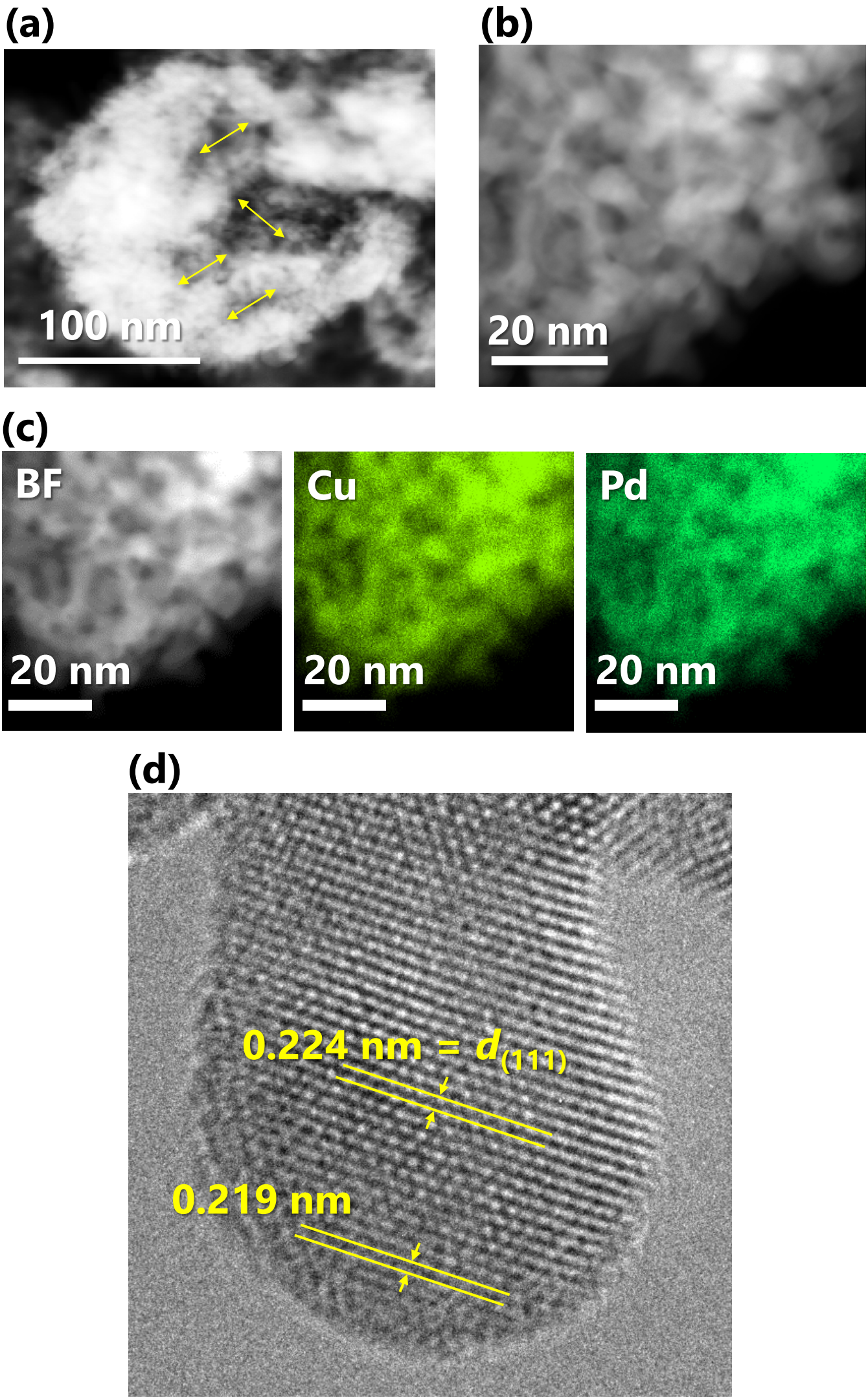
(a)
100 nm
(b)
20 nm
(c)
BF
20 nm
Cu
20 nm
Pd
20 nm
(d)
0.224 nm = $d_{(111)}$
0.219 nm

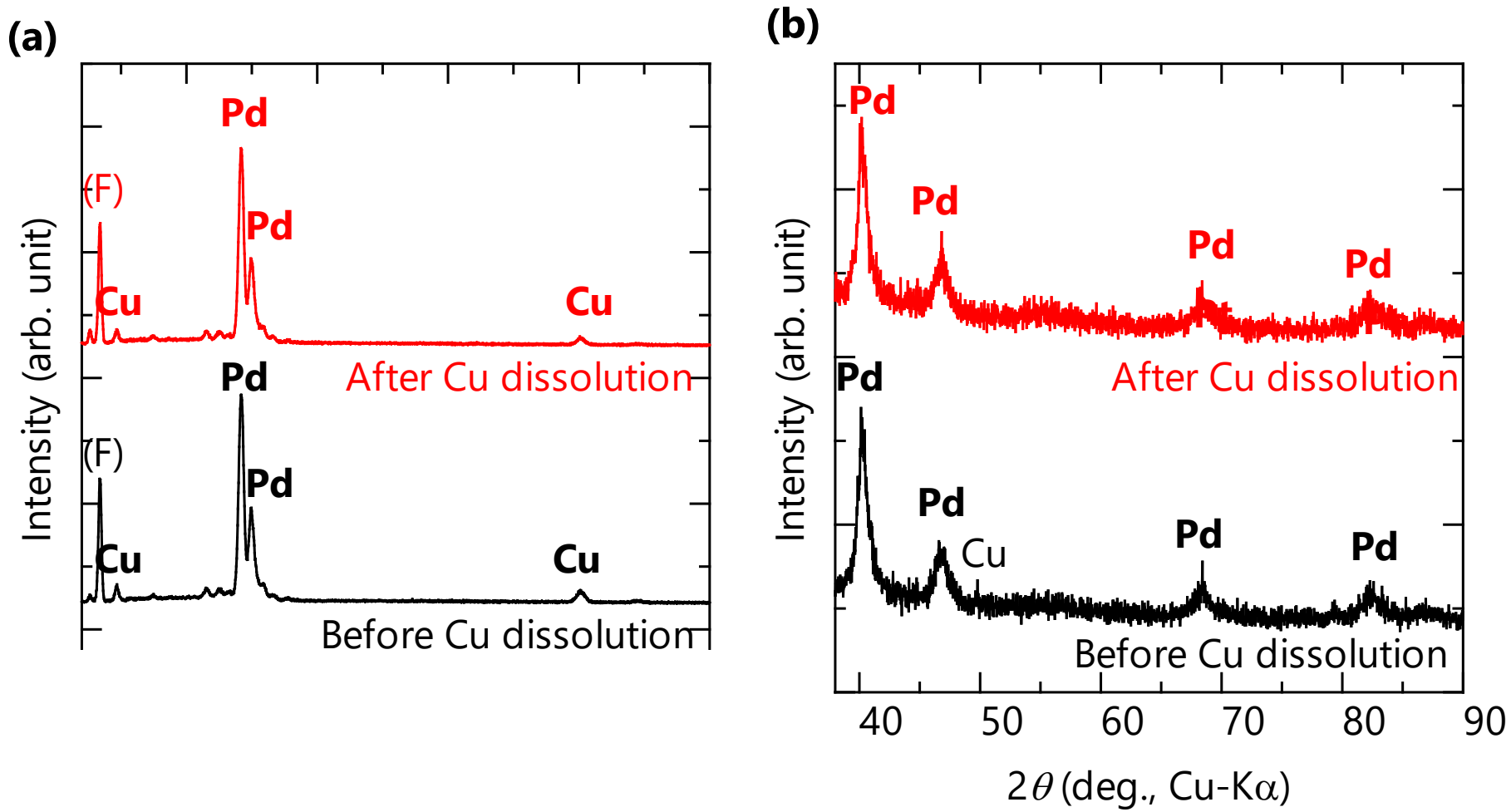
(a)
Intensity (arb. unit)
(F)
Pd
Pd
Cu
Cu
After Cu dissolution
Pd
(F)
Pd
Cu
Cu
Before Cu dissolution
(b)
Intensity (arb. unit)
Pd
Pd
Pd
Pd
After Cu dissolution
Pd
Pd
Cu
Pd
Pd
Before Cu dissolution
40
50
60
70
80
90
2θ (deg., Cu-Kα)

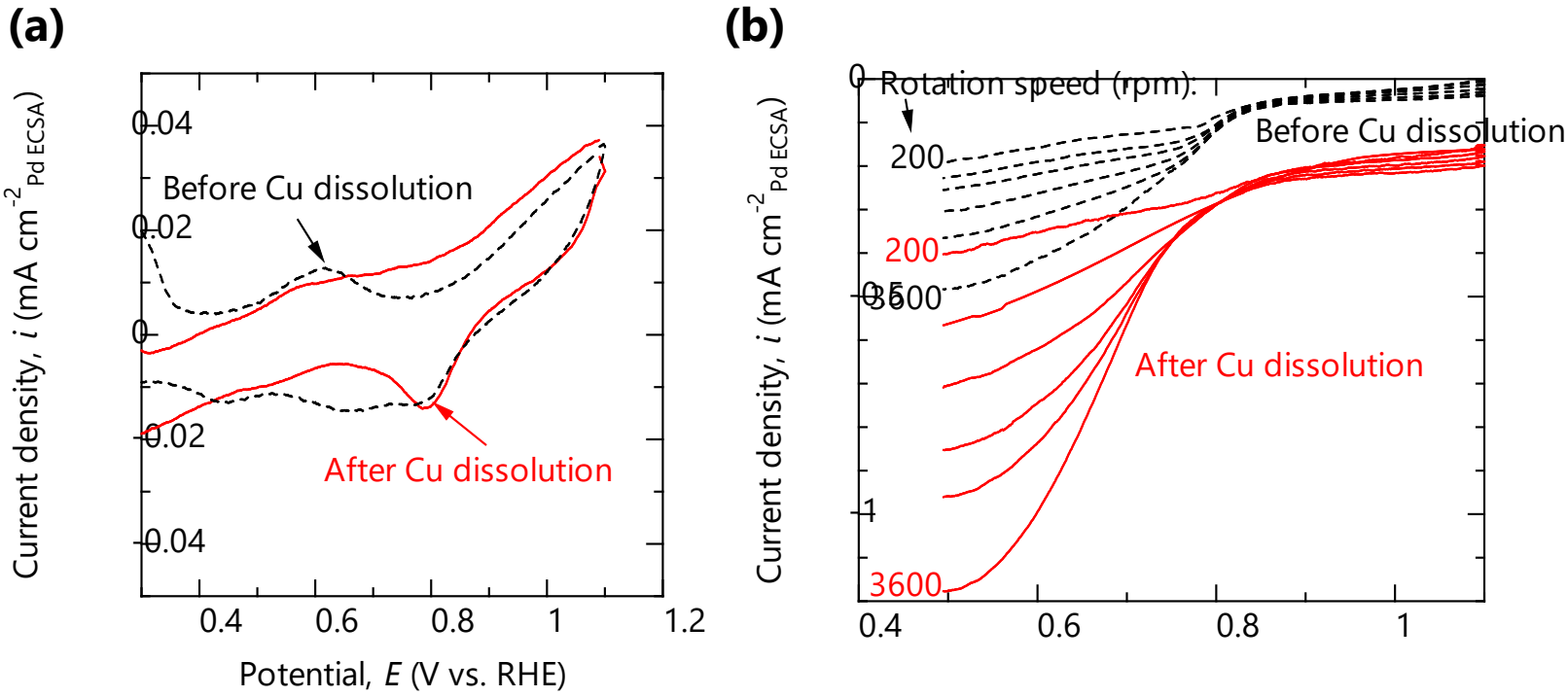
(a)
0.04
0.02
0
-0.02
-0.04
Before Cu dissolution
After Cu dissolution
Current density, i (mA cm-2 Pd ECSA)
0.4
0.6
0.8
1
1.2
Potential, E (V vs. RHE)
(b)
0
Rotation speed (rpm):
200
200
3600
3600
Before Cu dissolution
After Cu dissolution
Current density, i (mA cm-2 Pd ECSA)
-1
0.4
0.6
0.8
1

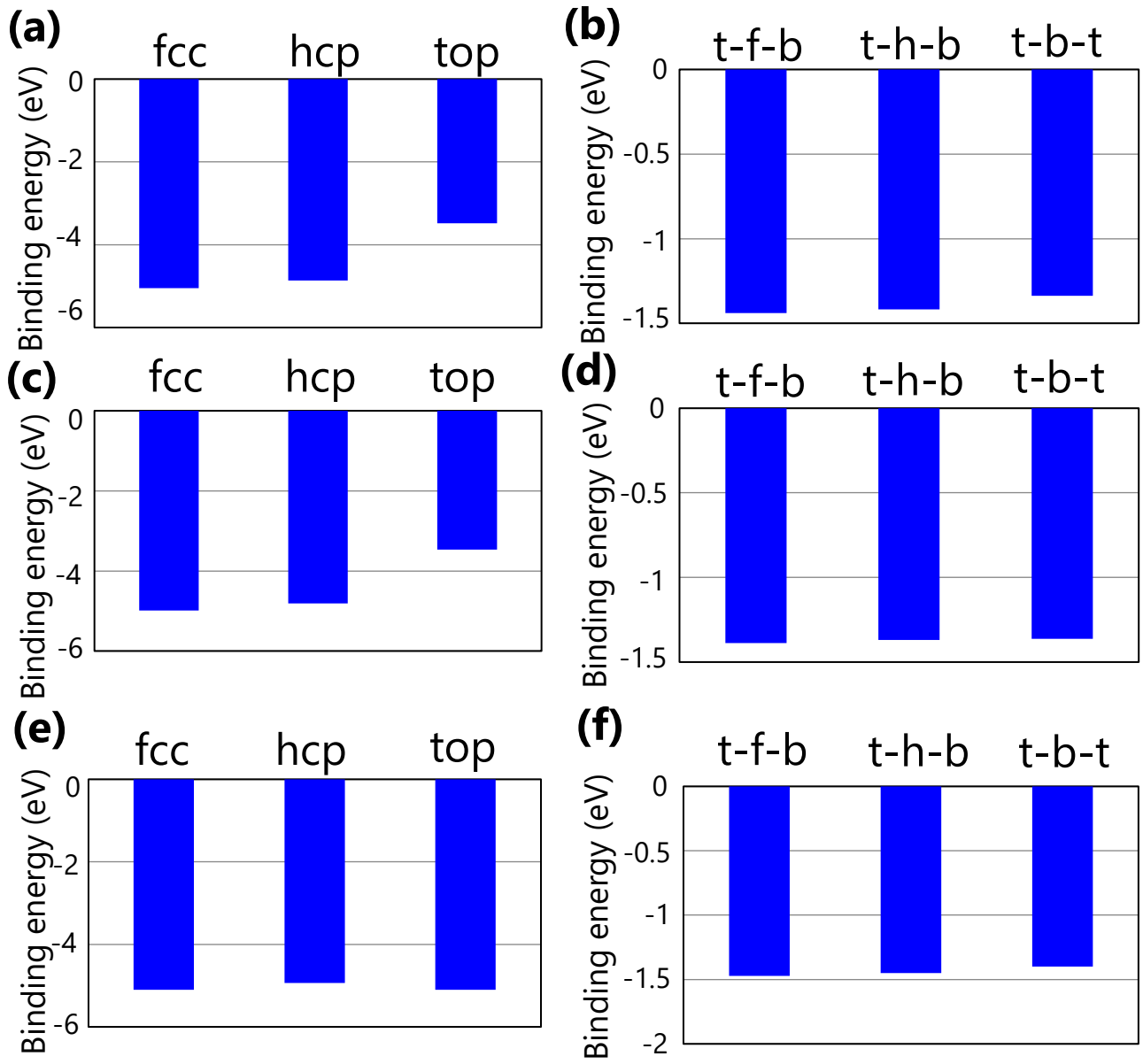
(a)
fcc
hcp
top
Binding energy (eV)
0
-2
-4
-6
(b)
t-f-b
t-h-b
t-b-t
Binding energy (eV)
0
-0.5
-1
-1.5
(c)
fcc
hcp
top
Binding energy (eV)
0
-2
-4
-6
(d)
t-f-b
t-h-b
t-b-t
Binding energy (eV)
0
-0.5
-1
-1.5
(e)
fcc
hcp
top
Binding energy (eV)
0
-2
-4
-6
(f)
t-f-b
t-h-b
t-b-t
Binding energy (eV)
0
-0.5
-1
-1.5
-2

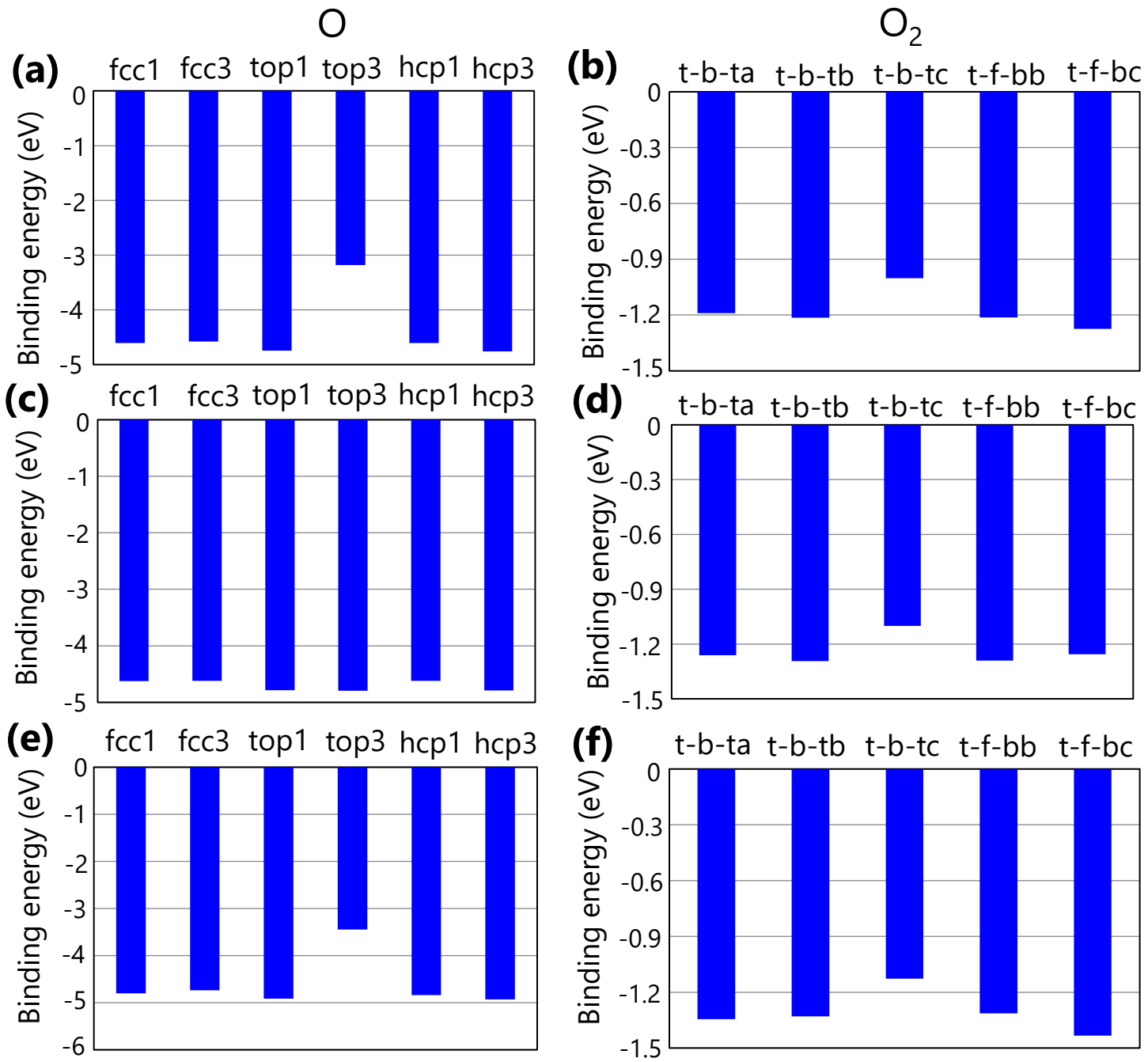
O
O_2
(a)
(b)
(c)
(d)
(e)
(f)
fcc1 fcc3 top1 top3 hcp1 hcp3
t-b-ta t-b-tb t-b-tc t-f-bb t-f-bc
Binding energy (eV)
0
-1
-2
-3
-4
-5
-6
-0.3
-0.6
-0.9
-1.2
-1.5

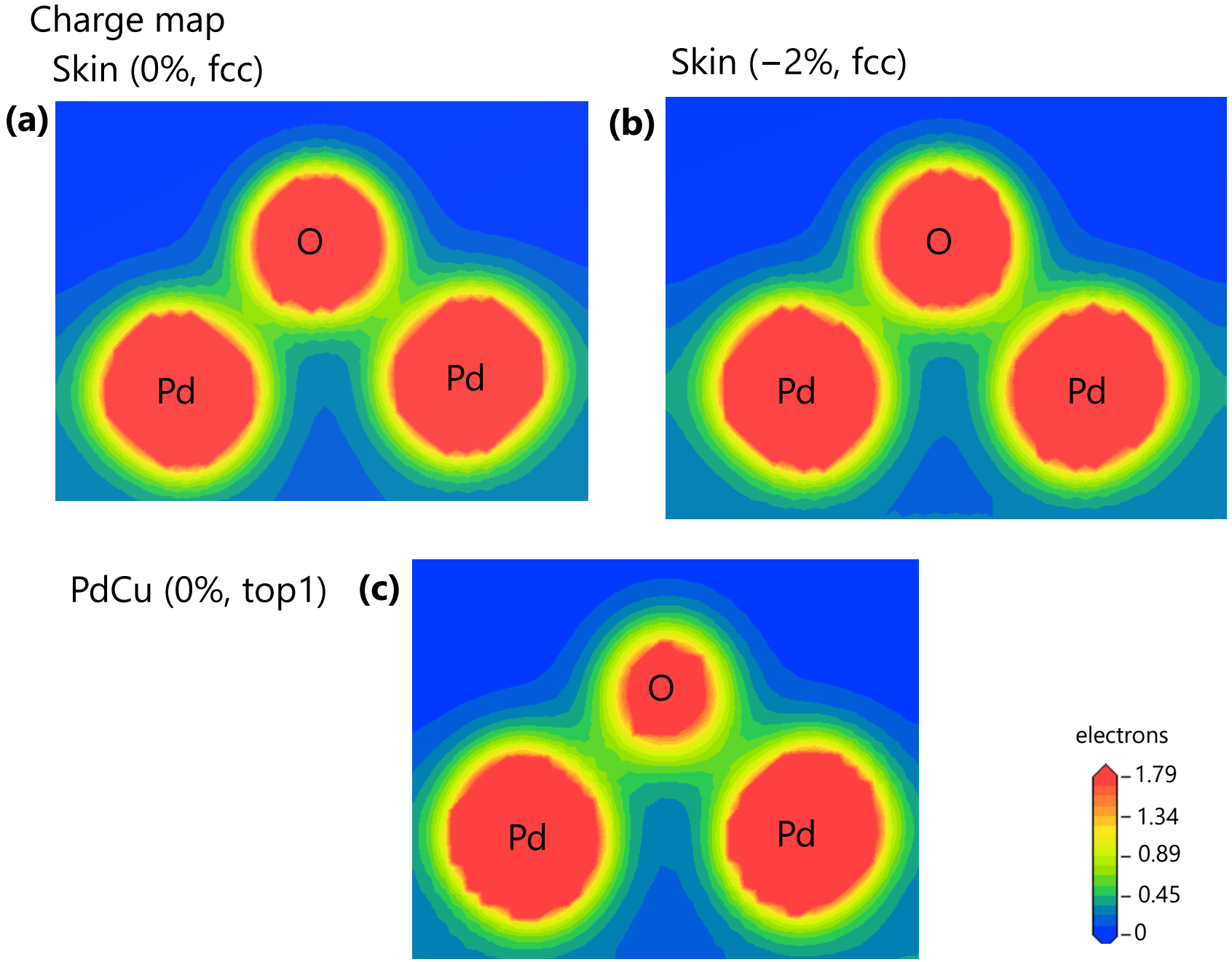
Charge map
Skin (0%, fcc)
(a)
O
Pd
Pd
Skin (−2%, fcc)
(b)
O
Pd
Pd
PdCu (0%, top1)
(c)
O
Pd
Pd
electrons
1.79
1.34
0.89
0.45
0

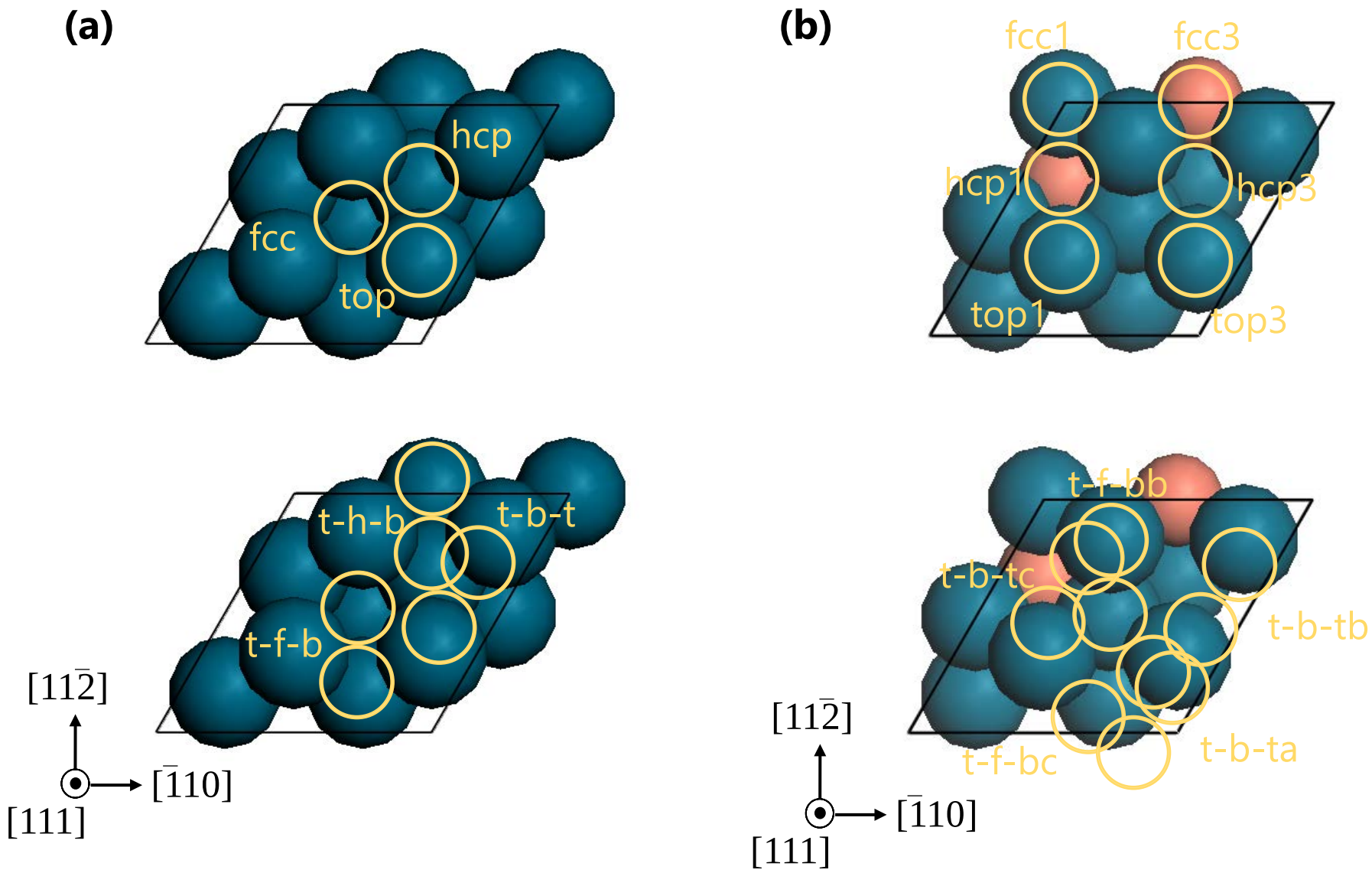
(a)
hcp
fcc
top
t-h-b
t-b-t
t-f-b
[11$\bar{2}$]
[$\bar{1}$10]
[111]
(b)
fcc1
fcc3
hcp1
hcp3
top1
top3
t-f-bb
t-b-tc
t-b-tb
t-f-bc
t-b-ta
[11$\bar{2}$]
[$\bar{1}$10]
[111]

Figure S1

skin

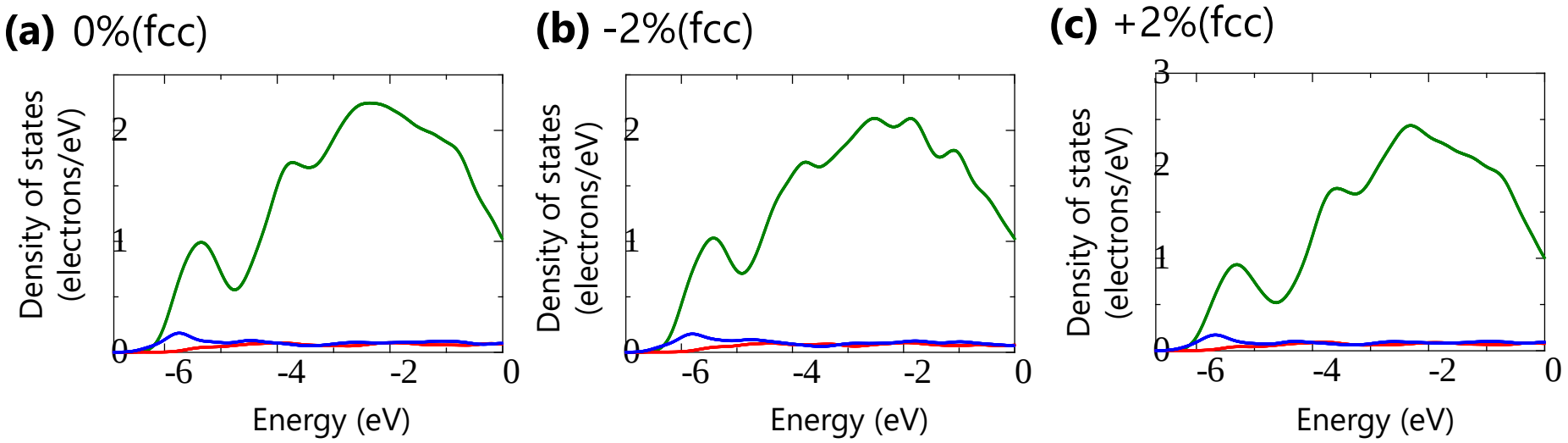

Cu

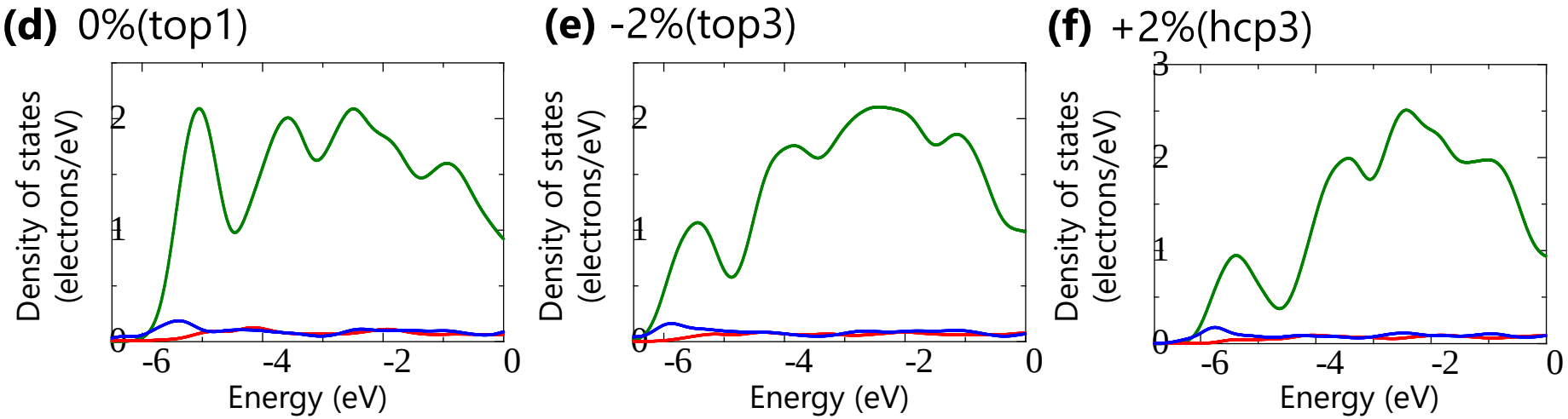

Figure S2

Supplemental Information for:

Oxygen reduction on bimodal nanoporous palladium-copper catalyst synthesized using sacrificial nanoporous copper

Naoki Miyazawa, Masataka Hakamada*, Yuto Sato and Mamoru Mabuchi

Department of Energy Science and Technology, Graduate School of Energy Science, Kyoto University, Yoshidahonmachi, Sakyo, 606-8501 Kyoto, Japan

* Corresponding author. E-mail: hakamada.masataka.3x@kyoto-u.ac.jp (M. Hakamada).

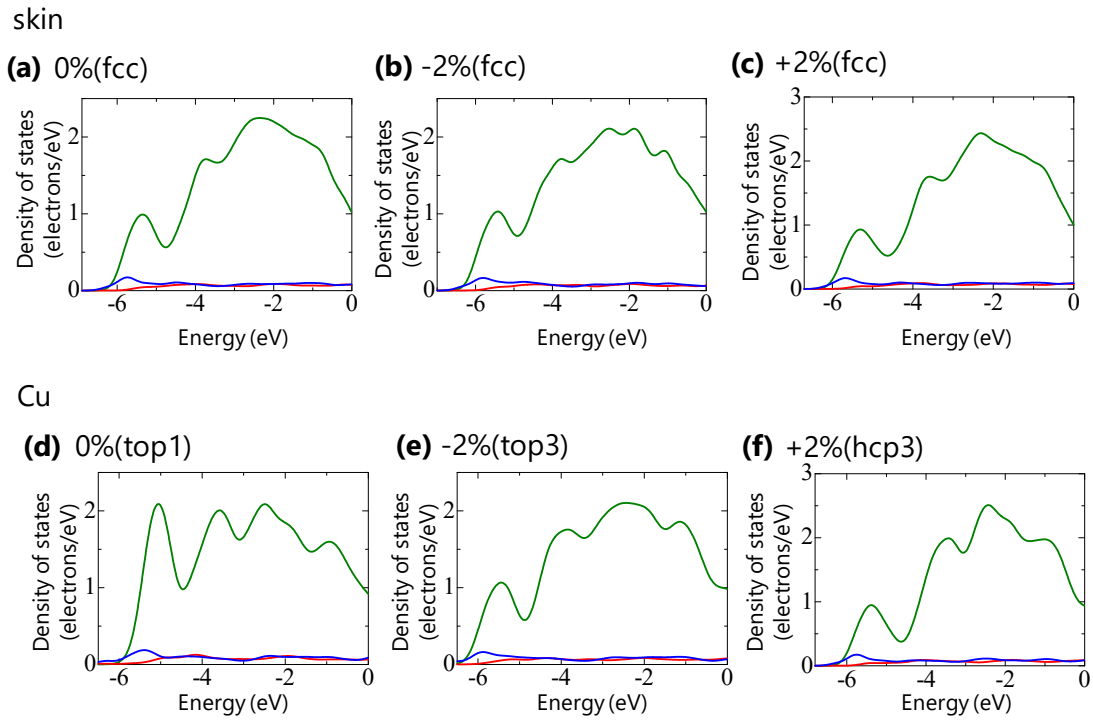

FIG. S1. Densities of states (DOS) for a palladium atom binding to an oxygen atom, (a) Pd surface with 0% strain, (b) Pd surface with 2% contraction strain, (c) Pd surface with 2% expansion strain, (d) Pd-Cu surface with 0% strain, (e) Pd-Cu surface with 2% contraction strain and (f) Pd-Cu surface with 2% expansion strain.

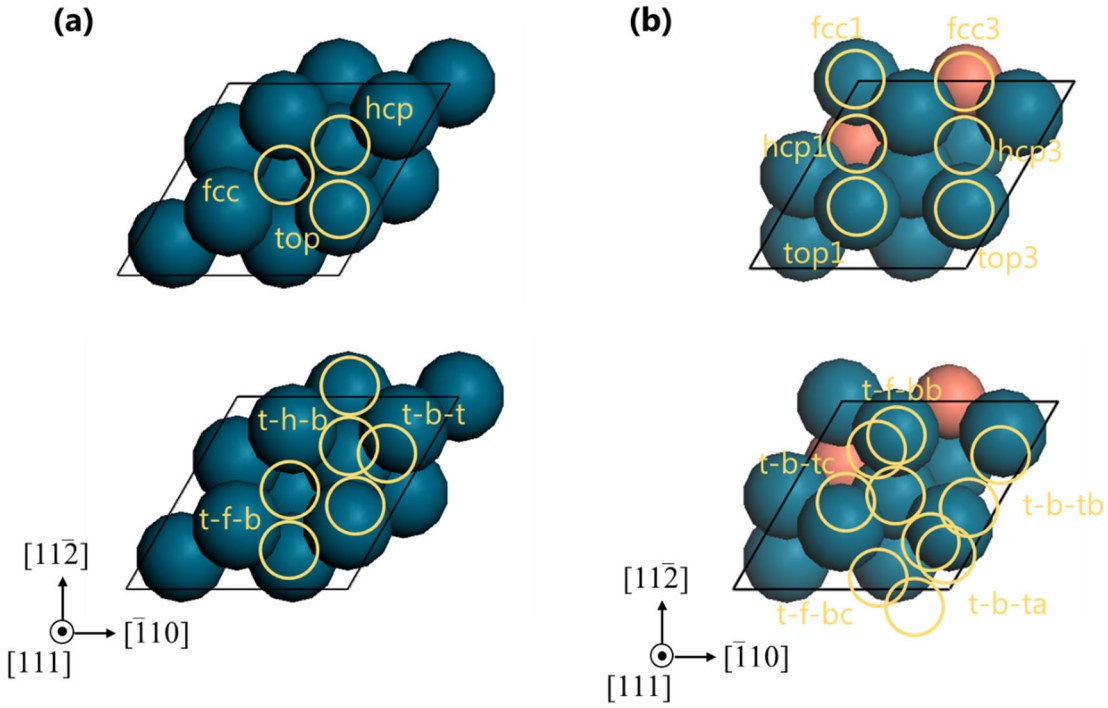

FIG. S2. Schematic illustration of models used for first-principles calculations, (a) Pd model and (b) Pd-Cu model. The blue and orange balls represent Pd and Cu atoms, respectively. The binding sites of O and O_2 species are shown by circles.